

Visible-to-ultraviolet frequency comb generation in lithium niobate nanophotonic waveguides

Received: 30 May 2023

Accepted: 4 December 2023

Published online: 15 January 2024

 Check for updates

Tsung-Han Wu^{1,2}, Luis Ledezma^{3,4}, Connor Fredrick^{1,2}, Pooja Sekhar^{1,2}, Ryoto Sekine³, Qiushi Guo³, Ryan M. Briggs⁴, Alireza Marandi³✉ & Scott A. Diddams^{1,2,5}✉

The introduction of nonlinear nanophotonic devices to the field of optical frequency comb metrology has enabled new opportunities for low-power and chip-integrated clocks, high-precision frequency synthesis and broad-bandwidth spectroscopy. However, most of these advances remain constrained to the near-infrared region of the spectrum, which has restricted the integration of frequency combs with numerous quantum and atomic systems in the ultraviolet and visible ranges. Here we overcome this shortcoming with the introduction of multisegment nanophotonic thin-film lithium niobate waveguides that combine engineered dispersion and chirped quasi-phase matching for efficient supercontinuum generation via the combination of $\chi^{(2)}$ and $\chi^{(3)}$ nonlinearities. With only 90 pJ of pulse energy at 1,550 nm, we achieve gap-free frequency comb coverage spanning 330–2,400 nm. The conversion efficiency from the near-infrared pump to the ultraviolet–visible region of 350–550 nm is 17%, and our modelling of optimized poling structures predicts an even higher efficiency. Harmonic generation via the $\chi^{(2)}$ nonlinearity in the same waveguide directly yields the carrier-envelope offset frequency and a means to verify the comb coherence at wavelengths as short as 350 nm. Our results provide an integrated photonics approach to create visible and ultraviolet frequency combs that will impact precision spectroscopy, quantum information processing and optical clock applications in this important spectral window.

Optical frequency combs offer a powerful tool for precise spectroscopic measurements using a broad array of spectrally equidistant and mutually coherent comb elements whose frequencies can be tied to absolute standards. In the two decades since the first near-infrared frequency combs were demonstrated, a tremendous range of scientific discovery and novel applications have been explored across the optical

spectrum—ranging from the terahertz (THz) to the ultraviolet (UV)^{1,2}. Still, efficient and reliable frequency comb coverage across the full visible and UV ranges has been challenging and is limiting multiple impactful research topics. For example, knowledge of the absolute UV frequency is critical to efficiently reach and reference the multiple trapping, cooling and state preparation transitions of atoms and ions

¹Time and Frequency Division, National Institute of Standards and Technology, Boulder, CO, USA. ²Department of Physics, University of Colorado, Boulder, CO, USA. ³Department of Electrical Engineering, California Institute of Technology, Pasadena, CA, USA. ⁴Jet Propulsion Laboratory, California Institute of Technology, Pasadena, CA, USA. ⁵Electrical Computer and Energy Engineering, University of Colorado, Boulder, CO, USA.

✉e-mail: marandi@caltech.edu; scott.diddams@colorado.edu

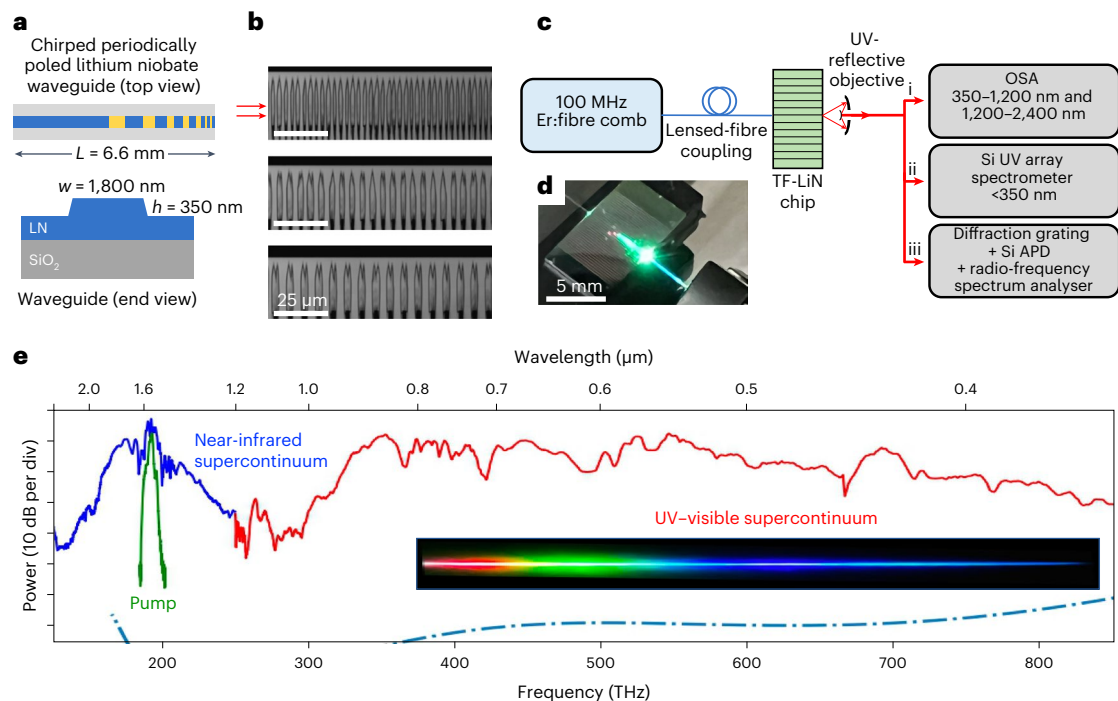


Fig. 1 | Nanophotonic LN waveguides for UV-to-near-infrared frequency comb generation. **a**, Schematic of the waveguide with a 3.0 mm unpoled segment that is followed by 3.6 mm poled period that linearly decreases from $\Lambda = 12.5$ to $2.5 \mu\text{m}$ (top). A cross-sectional schematic of the waveguide with dimensions of $w = 1,800 \text{ nm}$ (defined at the top of the waveguide) and $h = 350 \text{ nm}$ is shown (bottom). The LN slab thickness is 350 nm , and the sidewall has a 60° angle from the etching. **b**, Second-harmonic microscopy images of three poled regions of the waveguide with approximate periods of $2.7 \mu\text{m}$ (top), $5.0 \mu\text{m}$ (middle) and $7.1 \mu\text{m}$ (bottom). The two red arrows on the left side of the upper image indicate the approximate position at which the waveguides are subsequently etched along the length of the poled region. **c**, Experimental setup for comb generation

and characterization. A suite of three different instruments are used to measure the spectrum and verify the optical coherence of the comb at wavelengths below 350 nm . Si APD, silicon avalanche photodiode; OSA, optical spectrum analyser. **d**, Photograph of the waveguide generating white light. **e**, Supercontinuum generated with the nanophotonic waveguide. The input spectrum of the Er:fibre laser at $1.55 \mu\text{m}$ is shown by the green line. Broadband frequency comb spectra generated in the LN waveguide with chirped poling is shown in blue and red. The resolution of the spectrum analyser used for the visible-wavelength data is 2 nm and the dashed line indicates the noise floor of the analyser. The inset shows a photograph of the dispersed visible spectrum of the comb.

used in optical clocks, quantum computing and sensing^{3,4}. In addition, frequency combs with $10\text{--}30 \text{ GHz}$ mode spacing play an important role in astronomical spectrograph calibration for exoplanet science. However, among all the work in this field, an Earth–Sun analogue has still not been discovered. Doing so will require precision astronomical radial velocity measurements with $\leq 10 \text{ cm s}^{-1}$ precision over multiple years, which includes robust $>10 \text{ GHz}$ frequency combs across the peak of the solar spectrum from 400 to 650 nm (ref. 5). Finally, a broadband UV comb is central to high-precision spectroscopy aimed at characterizing and quantifying UV transitions in atmospheric gases and aerosols that are important in climate science⁶.

The lack of suitable laser gain media in the UV spectral region elevates the importance of nonlinear optical techniques to access this region. Upconversion using harmonic generation with noble gases^{7–10} and bulk crystals^{11–13} or supercontinuum broadening with waveguides^{14–20} or optical fibre²¹ are the most common methods to produce coherent UV frequency combs. However, those approaches have only partial spectral coverage or require intense pump pulses or cavity enhancement^{8,22,23}. This increases the complexity and noise through high power amplification and makes it unfeasible to realize UV coverage with gigahertz-rate frequency comb sources. Additionally, it has been observed that UV light can damage commonly used silica-based fibres and waveguides, such that the performance degrades on the timescale of hours to days¹⁵.

Here we introduce a novel engineered combination of nonlinear optical advances that provide efficient UV-to-visible gap-free frequency comb coverage. Instead of using the $\chi^{(3)}$ nonlinear process in

the anomalous dispersion regime, we leverage domain engineering and the strong $\chi^{(2)}$ nonlinearity in the normal dispersion regime of the lithium niobate (LN) nanophotonics platform. LN has a long history as one of the most widely used nonlinear optical materials, and recent developments in nanoscale fabrication open new opportunities to engineer waveguides for integrated supercontinuum and frequency comb generation at picjoule (pJ) and lower pulse energies^{18,24–27}. In recent work, techniques were introduced for the low-energy measurement of carrier-envelope offset frequency that take advantage of simultaneous $\chi^{(2)}$ and $\chi^{(3)}$ nonlinearities²⁶. However, in these cases, the continuous spectral bandwidth extends to approximately 600 nm , leaving at least 350 THz of the spectrum, at wavelengths in the UV, without spectral coverage. Except for a few notable cases of narrow-band phase-matched frequency conversion in material platforms like aluminium nitride¹⁹ and silica¹⁵, the visible and near-UV regions of the spectrum have been largely inaccessible for frequency combs generated with nonlinear nanophotonics.

Our work fills this extensive spectral gap with continuous UV-to-visible frequency comb coverage. This is accomplished with a novel multisegment nonlinear waveguide design in thin-film LN by combining the engineering of dispersion and quasi-phase matching. The initial segment consists of a low-dispersion waveguide that acts to spectrally broaden the $1,550 \text{ nm}$ pulses from a robust and technologically mature 100 MHz Er:fibre comb. The second segment includes the engineering of quasi-phase matching, which is poled with longitudinally chirped periods that enhance the generation of visible and near-UV signals via harmonic and cascaded $\chi^{(2)}$ processes.

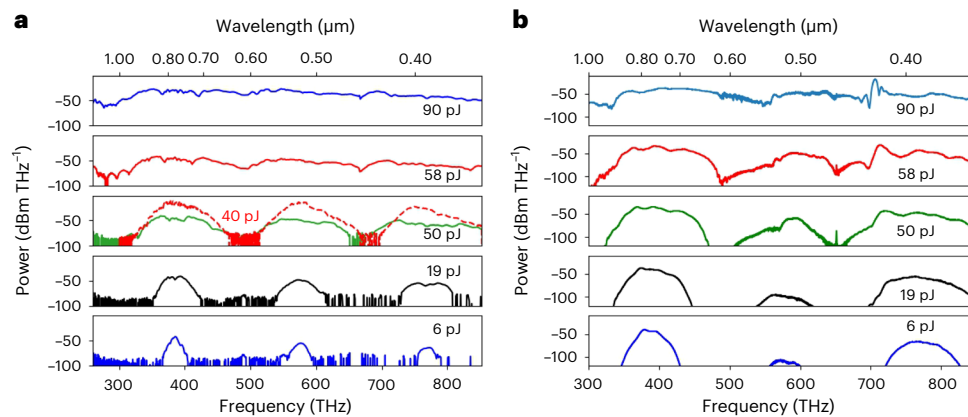


Fig. 2 | Spectral evolution of broad-bandwidth frequency comb generation. **a**, Experimental results of the power spectral density with input driving pulse energies between 6 and 90 pJ. All the data were taken with a pump source having a 100 MHz frequency comb, with the exception of the dashed red line at

40 pJ, which was obtained with a 10 GHz, 1,550 nm pump source. **b**, Simulation results at the same pulse energies, showing good qualitative agreement with the experimental data.

The combination of nanophotonic confinement and engineered dispersion and phase matching leads to exceptional efficiency, and our experiments show 17% of the 1,550 nm pulse energy can be translated to form a gap-free continuum in the spectral region of 350–550 nm. Low noise and optical coherence across 350 THz are verified by heterodyne measurements, revealing kilohertz-range relative linewidths and a noise floor near the shot-noise limit.

Our measurements are supported by numerical modelling with a single-envelope equation, yielding good agreement with experiments and the prediction of still greater increases in efficiency with optimized waveguide designs. Simulations further support preliminary measurements with 1,550 nm pulses at 10 GHz, illustrating a clear path to full visible-to-UV spectral coverage at $100\times$ greater repetition rate with <100 pJ pulses. Together, our results highlight the means to achieve compact and robust frequency comb coverage across spectral bands critical for challenging and impactful applications in quantum sensing and computing, precision astronomical spectroscopic calibration and broad-bandwidth frequency comb spectroscopy. Furthermore, similar design strategies can be implemented for coherent frequency comb spectra across the full transparency window of LN, namely, from 330 nm to 5 μm .

Experiment

Figure 1 shows the important details of our experiments and the nanophotonic LN waveguides we employ. Figure 1a depicts the waveguides that are etched from a 710 nm film of LN on oxide to be 350 nm high and 1,800 nm wide, with a 1,550 nm mode area of approximately $1\ \mu\text{m}^2$. The waveguide dispersion at 1,550 nm is calculated to be slightly anomalous and increases to a large normal value below 1,000 nm (Supplementary Fig. 1). In the longitudinal direction, we introduce a segmented structure with 3 mm of an unpoled region of the waveguide. This is followed by 3.6 mm in which we implement a chirp in the poling period Λ , which linearly decreases along the propagation direction from $\Lambda = 12.5$ to 2.5 μm . Figure 1b shows the two-photon microscopy images of the poled regions of the LN before etching of the waveguides. Instead of the more typical supercontinuum in anomalous dispersion, the 3 mm section employs $\chi^{(3)}$ self-phase modulation to spectrally broaden the input pulse, whereas the chirped poling in the second section expands the near-infrared light to the visible and UV regions via $\chi^{(2)}$ and cascaded $\chi^{(2)}$ nonlinear processes. The evolution of the spectral broadening is discussed further below.

The experimental setup is depicted in Fig. 1c, including the pump laser source and diagnostics. We pump the waveguide with 1,550 nm

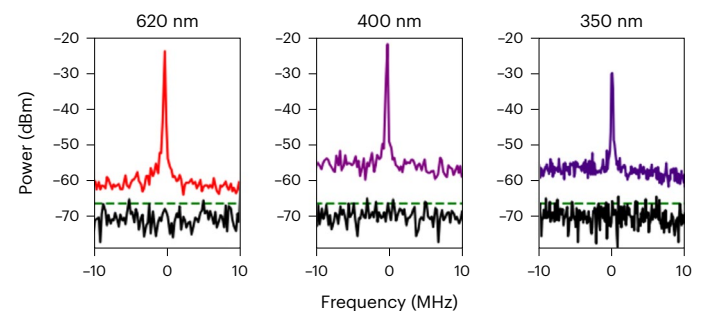


Fig. 3 | Broad-bandwidth coherence and carrier-envelope offset frequency detection. The f_{ceo} beatnote is directly observed at wavelengths across the visible and UV ranges. The signal-to-noise ratios of f_{ceo} at 620 and 400 nm are both greater than 35 dB in 10 kHz resolution bandwidth. The signal-to-noise ratio at 350 nm is about 28 dB. The green dashed line is the shot noise and the black line is the measurement noise floor.

pulses from a 100 MHz Er:fibre frequency comb that is amplified to produce pulses with duration near the Fourier-transform limit of ~ 130 fs, and with 100 mW of average power. The power incident on the waveguide is varied without changing the pulse duration and a polarization-maintaining lensed fibre is used for the input coupling. We estimate a coupling loss of 10 dB at each facet, such that 9 mW is coupled into the waveguide when pumped with 90 mW. Under these conditions, continuous spectral coverage extending from the near-infrared pump to the UV is achieved (Fig. 1e). The bandwidth at 30 dB below the peak of the visible spectrum is 555 THz. The extremely broad nature of the output spectrum requires that the output coupling be done with a reflective microscope objective that has low loss into the UV. The inset in Fig. 1e shows a photograph of the visible spectrum after dispersing the collimated output with a diffraction grating.

The progression of the spectral expansion with input pulse energy is shown in Fig. 2, where the experimental and simulated spectra are presented side by side. The input-pulse bandwidth is broadened from 30 to 400 nm in the first 3 mm of the unpoled waveguide (Fig. 1c). In the next 3.6 mm, the $\chi^{(2)}$ nonlinearity generates the second harmonic ($2f$, 384 THz, 780 nm), third harmonic ($3f$, 576 THz, 520 nm) and fourth harmonic ($4f$, 770 THz, 390 nm) with a driving pulse energy of less than 10 pJ. As the pulse energy increases to tens of picojoules, our simulations show that the spectral broadening is significantly enhanced in the poled region. In particular, for pulse energies higher than 50 pJ, the

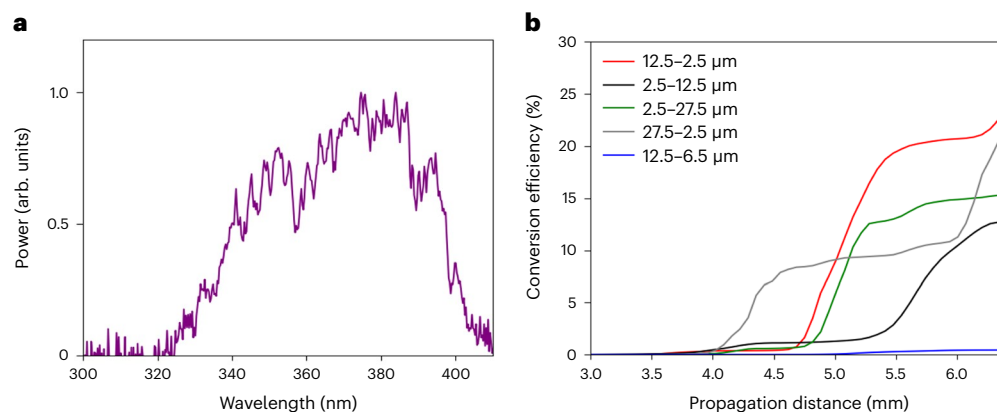


Fig. 4 | UV spectral limits and efficiency. **a**, UV spectrum produced with the waveguide shown in Fig. 1a, and measured after a UV bandpass filter to eliminate any light at longer wavelengths. The short-wavelength cutoff of the spectrum is consistent with absorption at the band edge of MgO-doped LN. **b**, Simulation

showing the integrated power (350–550 nm) along the waveguide propagation direction. Each curve is from a different simulation in which the linear chirp rate and range were varied to illustrate the design capabilities.

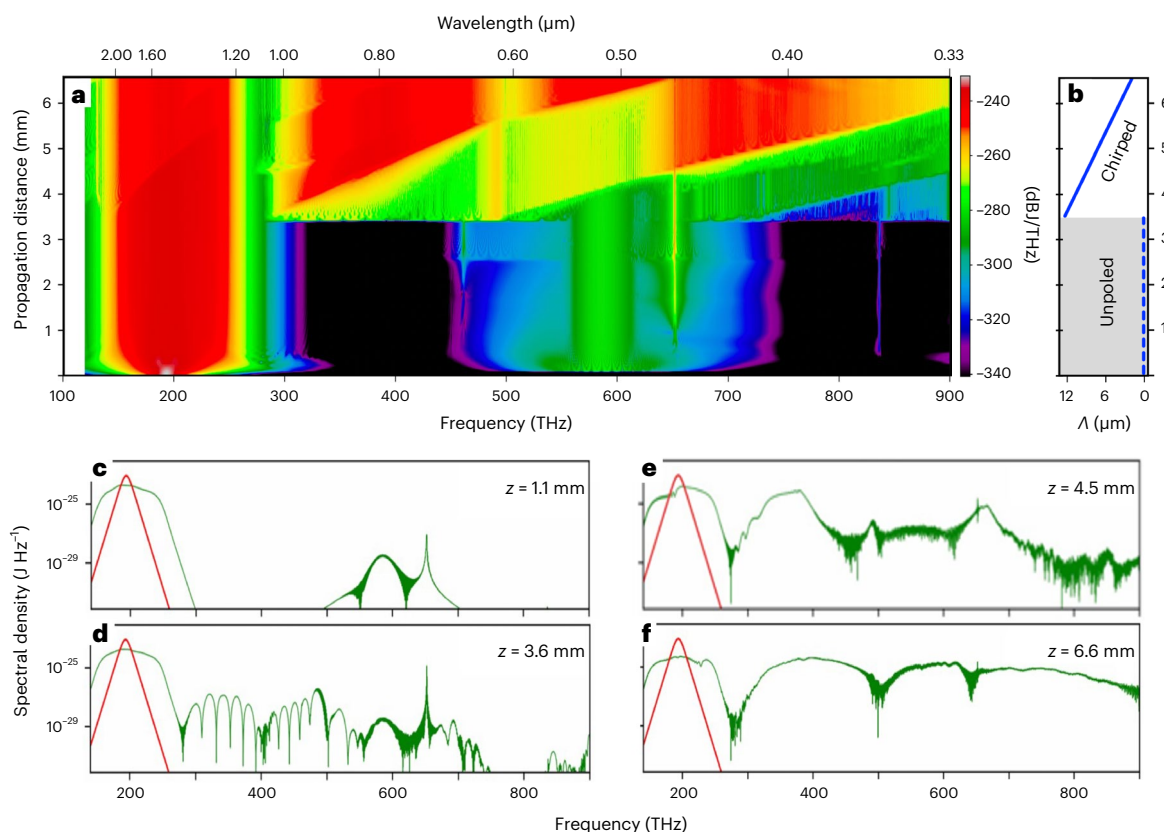


Fig. 5 | Nonlinear spectral evolution in thin-film LN waveguides with $\chi^{(3)}$ and $\chi^{(2)}$ nonlinearities. **a**, Simulation of the spectral evolution as a function of pulse propagation distance. **b**, Map of the poling period (Λ) along the same propagation distance. Chirped poling starts at 3.6 mm and linearly decreases from $\Lambda = 12.5 \mu\text{m}$ to $2.5 \mu\text{m}$. **c–f**, Plots of the spectrum at different propagation distances. The input spectrum for the simulation is shown in red. The broadening

of the input spectrum via the $\chi^{(3)}$ nonlinearity and non-phase-matched third-harmonic frequency of the pump (**c**). The spectrum at the beginning of the linearly chirped poling region of the waveguide (**d**). The visible spectrum is continually generated and spectrally broadened from the harmonic bands and the combination of $\chi^{(2)}$ effects (**e,f**).

spectral regions around $2f$, $3f$ and $4f$ start to overlap, and with $\sim 90 \text{ pJ}$ (9 mW on chip), the spectrum is continuous and gap free from 350 to 1,000 nm. The progression is reflected in the simulations shown in Fig. 2b, which employ a unidirectional propagation equation^{28,29}. Methods provides further details of the modelling. Over the full range of energies

and spectral bandwidths, we see excellent agreement between the measurements and simulations in terms of the spectral coverage, spectral shape and required pulse energy. As discussed below and in Supplementary Fig. 2, this level of agreement provides the basis for design improvements aimed at spectrally tailored frequency combs

for optical clocks, astronomical spectrograph calibration and spectroscopic sensing.

In addition to UV and visible comb generation at 100 MHz, we implement the same waveguide shown in Fig. 1a to demonstrate visible comb generation when pumped with the output of a 10 GHz resonant electro-optic frequency comb³⁰. Frequency combs in the range of 10 GHz are of interest for astronomical spectrograph calibration, but broad-bandwidth coverage at a 100× higher repetition rate is challenging because of the corresponding decrease in pulse energy for the same average power. The data with the 10 GHz pump source (Fig. 2a, dashed line) shows the spectrum of the second, third and fourth harmonics with about 40 pJ (400 mW) of 50 fs pulses coupled into the waveguide. These data are consistent with the 100 MHz data and simulations, with spectral bandwidth falling between the plots for 19 and 50 pJ. For this experiment, the UV intensity out of the waveguide was attenuated due to a non-optimized output coupling into a multi-mode fibre of 1 m length. Even though the spectrum does not cover the full UV and visible ranges, the fourth harmonic power in the UV is still estimated to be on the order of 1–5 μW per comb mode. We see no damage to the nanophotonic waveguides, even with about 2.5 W of incident power at 10 GHz. With coupling losses reduced to 1–2 dB, as demonstrated by others^{31,32}, it should be possible to achieve continuous 10 GHz spectral coverage across the visible and UV with a little over 1 W of incident power.

The spectral overlap between the harmonics provides the means to detect the carrier-envelope offset frequency f_{ceo} of the driving comb, as well as to verify the coherence of the comb structure. This is accomplished by diffracting the output spectrum with a grating and detecting various regions of the spectrum with a Si avalanche photodiode (Fig. 1c). Figure 3 shows the f_{ceo} values detected at 620, 400 and 350 nm. At longer wavelengths of 620 and 400 nm, the signal-to-noise ratio is greater than 35 dB in 10 kHz resolution bandwidth. The heterodyne beatnote in the UV (350 nm) provides direct evidence of the coherence of the ultrabroad frequency comb generated with this unique chirped poling in thin-film LN waveguides. It is the presence of multiple frequency combs that leads to the observed f_{ceo} . Although for some applications, this could introduce complications, these offsets could be easily eliminated by making $f_{\text{ceo}} = 0$ for the entire comb^{33,34}. We note that in spectroscopic situations, the presence of a secondary comb provides a means for measuring and controlling f_{ceo} with a single detector^{35,36}.

As shown in Fig. 3, the noise floor is near the shot-noise limit, but includes some excess noise. It is common for such excess noise to originate from the amplified 1,550 nm Er:fibre laser, which is not shot noise limited, but it could be further amplified during nonlinear propagation in the waveguide. The noise-generating processes in such massive spectral broadening with $\chi^{(2)}$ and $\chi^{(3)}$ nonlinearities remains an important future research topic. This is of further interest for the 10 GHz electro-optic comb, for which previous work with only $\chi^{(3)}$ spectral broadening has required additional mitigation of the multiplied radio-frequency to achieve coherence³⁷.

To more accurately quantify the UV extent of the frequency comb, we additionally measured its spectrum using a Si-based array spectrometer in conjunction with a UV bandpass filter (maximum wavelength, 400 nm). The result is shown in Fig. 4. Evidently, the generated spectrum extends to below 330 nm. We believe this is the shortest-wavelength supercontinuum or harmonic generation in any LN platform. The UV extent of the spectrum is consistent with the bandgap of MgO-doped lithium, which has been reported to be in the range of 3.4–3.9 eV (approximately 320–360 nm)^{38–40}. We independently measured the average on-chip power of the UV–visible spectrum (350–550 nm) to be 1.5 mW with 9.0 mW (90 pJ) of on-chip pump power. This implies an impressive 17% conversion efficiency from the 1,550 nm pump to the UV–visible spectrum. The conversion from 1,550 nm to these shorter wavelengths can be controlled and enhanced by the linear chirp range and chirp rate. This is shown in Fig. 4b, where we present our

predictions of the integrated power of light spanning 350–550 nm with different poling conditions. For the parameters of the waveguides that we have employed in the experiments, these simulation results show that the ideal efficiency can be near 22%. Additional optimization of the waveguides can potentially yield efficiencies of >30% over specific wavelength regions (Supplementary Fig. 2).

Discussion and conclusion

Complex nonlinear interactions give rise to the broad-bandwidth spectra across the visible and near-UV regimes. However, as we discuss here, these interactions can be understood and subsequently tailored to optimize the supercontinuum generation. Different from the majority of other approaches, the devices we have fabricated rely most strongly on the $\chi^{(2)}$ nonlinearity and the engineered $\chi^{(3)}$ that arises from the cascading of the $\chi^{(2)}$ process. The strong $\chi^{(2)}$ nonlinearity gives rise to efficient spectral broadening in the visible and near-UV regimes where phase matching via $\chi^{(3)}$ is challenging due to the rapidly increasing normal dispersion.

Figure 5 shows a simulation that illustrates the evolution of spectral broadening as a function of the propagation distance. The supercontinuum generation in the LN waveguide begins with engineered waveguide dispersion close to zero at 1,550 nm. In this unpoled section of the waveguide, self-phase modulation rapidly broadens the fundamental pulse at 1,550 nm (Fig. 5c). Third-harmonic generation is also seen in this section of the waveguide. Once the pulse enters the chirped poling section of the waveguide, the second-harmonic generation increases from lower frequency to high frequency, and is followed in a similar fashion by fourth-harmonic generation (Fig. 5d–f). Finally, the spectrum in the third-harmonic region that was initially produced in the unpoled region then grows by the mixing of second-harmonic and fundamental frequencies. Throughout the propagation in the poled region, we observe further spectral broadening across the entire visible and UV ranges akin to effective $\chi^{(3)}$ via the cascading of the second-order nonlinearity. This broadened spectrum is shown in Fig. 5f.

To summarize, we have demonstrated a multisegment nanophotonic LN waveguide that combines both dispersion and quasi-phase-matching engineering. This novel design leverages the interaction between $\chi^{(2)}$ and $\chi^{(3)}$ nonlinearities to generate continuous frequency comb spectra extending from 330 to 2,400 nm with less than 100 pJ energy. This is accomplished with pumping at the wavelength of 1,550 nm using mature Er:fibre laser technology. Furthermore, the coherence of the supercontinuum is verified by measuring f_{ceo} from the UV spectrum. Our results highlight the path to further enhance the interaction between $\chi^{(3)}$ and $\chi^{(2)}$ nonlinearities and enhance efficient visible and UV spectral generation. As discussed in Supplementary Fig. 2, optimized designs with additional high-frequency poling in the first section of the waveguide can increase the conversion from 1,550 nm into the UV with efficiency greater than 32%. Besides varying the length of the unpoled section, engineering the dispersion of waveguide can extend the bandwidth into the mid-infrared regime with intrapulse or dual-band difference-frequency generation. By engineering the phase (mis)match in $\chi^{(2)}$ and $\chi^{(3)}$ effects in nanophotonic LN waveguides, it is now possible to generate a compact light source with coverage across the full transparency window of LN— from approximately 330 to 5,000 nm. Such design control will open new opportunities with the thin-film LN platform for applications of spectroscopy and trace gas sensing, control of quantum systems and atomic clocks.

Online content

Any methods, additional references, Nature Portfolio reporting summaries, source data, extended data, supplementary information, acknowledgements, peer review information; details of author contributions and competing interests; and statements of data and code availability are available at <https://doi.org/10.1038/s41566-023-01364-0>.

References

- Diddams, S. A., Vahala, K. & Udem, T. Optical frequency combs: coherently uniting the electromagnetic spectrum. *Science* **369**, eaay3676 (2020).
- Fortier, T. & Baumann, E. 20 years of developments in optical frequency comb technology and applications. *Commun. Phys.* **2**, 153 (2019).
- Ludlow, A. D., Boyd, M. M., Ye, J., Peik, E. & Schmidt, P. Optical atomic clocks. *Rev. Mod. Phys.* **87**, 637–701 (2015).
- Haffner, H., Roos, C. & Blatt, R. Quantum computing with trapped ions. *Phys. Rep.* **469**, 155–203 (2008).
- Fischer, D. et al. State of the field: extreme precision radial velocities. *Publ. Astron. Soc. Pac.* **128**, 066001 (2016).
- Galtier, S., Pivard, C. & Rairoux, P. Towards DCS in the UV spectral range for remote sensing of atmospheric trace gases. *Remote Sens.* **12**, 3444 (2020).
- Kandula, D. Z., Gohle, C., Pinkert, T. J., Ubachs, W. & Eikema, K. S. E. Extreme ultraviolet frequency comb metrology. *Phys. Rev. Lett.* **105**, 063001 (2010).
- Pupeza, I., Zhang, C., Högner, M. & Ye, J. Extreme-ultraviolet frequency combs for precision metrology and attosecond science. *Nat. Photon.* **15**, 175–186 (2021).
- Gohle, C. et al. A frequency comb in the extreme ultraviolet. *Nature* **436**, 234–237 (2005).
- Jones, R. J., Moll, K. D., Thorpe, M. J. & Ye, J. Phase-coherent frequency combs in the vacuum ultraviolet via high-harmonic generation inside a femtosecond enhancement cavity. *Phys. Rev. Lett.* **94**, 193201 (2005).
- Yang, K. et al. High-power ultra-broadband frequency comb from ultraviolet to infrared by high-power fiber amplifiers. *Opt. Express* **20**, 12899–12905 (2012).
- Lesko, D. M. B. et al. A six-octave optical frequency comb from a scalable few-cycle erbium fibre laser. *Nat. Photon.* **15**, 281–286 (2021).
- Lesko, D. M. B., Chang, K. F. & Diddams, S. A. High-sensitivity frequency comb carrier-envelope-phase metrology in solid state high harmonic generation. *Optica* **9**, 1156–1162 (2022).
- Iwakuni, K. et al. Generation of a frequency comb spanning more than 3.6 octaves from ultraviolet to mid infrared. *Opt. Lett.* **41**, 3980–3983 (2016).
- Oh, D. Y. et al. Coherent ultra-violet to near-infrared generation in silica ridge waveguides. *Nat. Commun.* **8**, 13922 (2017).
- Herr, S. J. et al. Frequency comb up- and down-conversion in synchronously driven $\chi^{(2)}$ optical microresonators. *Opt. Lett.* **43**, 5745–5748 (2018).
- Rutledge, J. et al. Broadband ultraviolet-visible frequency combs from cascaded high-harmonic generation in quasi-phase-matched waveguides. *J. Opt. Soc. Am. B* **38**, 2252–2260 (2021).
- Reig Escalé, M., Kaufmann, F., Jiang, H., Pohl, D. & Grange, R. Generation of 280 THz-spanning nearultraviolet light in lithium niobate-on-insulator waveguides with sub-100 pJ pulses. *APL Photonics* **5**, 121301 (2020).
- Liu, X. et al. Beyond 100 THz-spanning ultraviolet frequency combs in a non-centrosymmetric crystalline waveguide. *Nat. Commun.* **10**, 2971 (2019).
- Nakamura, K., Kashiwagi, K., Okubo, S. & Inaba, H. Erbium-doped-fiber-based broad visible range frequency comb with a 30 GHz mode spacing for astronomical applications. *Opt. Express* **31**, 20274–20285 (2023).
- Mridha, M. K., Novoa, D., Bauerschmidt, S. T., Abdolvand, A. & Russell, P. S. Generation of a vacuum ultraviolet to visible Raman frequency comb in H₂-filled kagomé photonic crystal fiber. *Opt. Lett.* **41**, 2811–2814 (2016).
- Peters, E. et al. A deep-UV optical frequency comb at 205 nm. *Opt. Express* **17**, 9183–9190 (2009).
- Pinkert, T. J. et al. Widely tunable extreme UV frequency comb generation. *Opt. Lett.* **36**, 2026–2028 (2011).
- Honardoost, A., Abdelsalam, K. & Fathpour, S. Rejuvenating a versatile photonic material: thin-film lithium niobate. *Laser Photonics Rev.* **14**, 2000088 (2020).
- Jankowski, M. et al. Ultrabroadband nonlinear optics in nanophotonic periodically poled lithium niobate waveguides. *Optica* **7**, 40–46 (2020).
- Okawachi, Y. et al. Chip-based self-referencing using integrated lithium niobate waveguides. *Optica* **7**, 702–707 (2020).
- Roy, A. et al. Visible-to-mid-IR tunable frequency comb in nanophotonics. *Nat. Commun.* **14**, 6549 (2023).
- François, P. L. Nonlinear propagation of ultrashort pulses in optical fibers: total field formulation in the frequency domain. *J. Opt. Soc. Am. B* **8**, 276–293 (1991).
- Kolesik, M. & Moloney, J. V. Nonlinear optical pulse propagation simulation: from Maxwell's to unidirectional equations. *Phys. Rev. E* **70**, 036604 (2004).
- Sekhar, P., Fredrick, C., Carlson, D. R., Newman, Z. & Diddams, S. A. 20 GHz fiber-integrated femtosecond pulse and supercontinuum generation with a resonant electro-optic frequency comb. *APL Photonics* **8**, 116111 (2023).
- He, L. et al. Low-loss fiber-to-chip interface for lithium niobate photonic integrated circuits. *Opt. Lett.* **44**, 2314–2317 (2019).
- Hu, C. et al. High-efficient coupler for thin-film lithium niobate waveguide devices. *Opt. Express* **29**, 5397–5406 (2021).
- Jones, D. et al. Carrier-envelope phase control of femtosecond mode-locked lasers and direct optical frequency synthesis. *Science* **288**, 635–639 (2000).
- Okubo, S., Onae, A., Nakamura, K., Udem, T. & Inaba, H. Offset-free optical frequency comb self-referencing with an $f-2f$ interferometer. *Optica* **5**, 188–192 (2018).
- Lind, A. J. et al. Mid-infrared frequency comb generation and spectroscopy with few-cycle pulses and $\chi^{(2)}$ nonlinear optics. *Phys. Rev. Lett.* **124**, 133904 (2020).
- Hoghooghi, N. et al. Broadband 1-GHz mid-infrared frequency comb. *Light Sci. Appl.* **11**, 264 (2022).
- Carlson, D. R. et al. Ultrafast electro-optic light with subcycle control. *Science* **361**, 1358–1363 (2018).
- Syuy, A. et al. Optical properties of lithium niobate crystals. *Optik* **156**, 239–246 (2018).
- Bhatt, R. et al. Studies on nonlinear optical properties of ferroelectric MgO-LiNbO₃ single crystals. *Ferroelectrics* **323**, 165–169 (2005).
- Bhatt, R. et al. Control of intrinsic defects in lithium niobate single crystal for optoelectronic applications. *Crystals* **7**, 23 (2017).

Publisher's note Springer Nature remains neutral with regard to jurisdictional claims in published maps and institutional affiliations.

Springer Nature or its licensor (e.g. a society or other partner) holds exclusive rights to this article under a publishing agreement with the author(s) or other rightsholder(s); author self-archiving of the accepted manuscript version of this article is solely governed by the terms of such publishing agreement and applicable law.

© The Author(s), under exclusive licence to Springer Nature Limited 2024

Methods

Waveguide fabrication

We use a commercially available X-cut wafer (NANOLN), with an ~700-nm-thick LN layer on top of an ~4.7- μm -thick silica buffer layer. We first deposit electrodes by electron-beam evaporation (15 nm Cr + 50 nm Au) for periodic poling. We apply an ~700 V pulse over a 25 μm gap to produce domain inversion. The poling period linearly decreases from $\Lambda = 12.5 \mu\text{m}$ to 2.5 μm along 3.6 mm length. Due to lateral domain growth during the poling process, the duty cycle for the metallic electrodes needs to be adjusted to obtain a 50% duty cycle along the poled length. Since this effect is more acute for shorter poling periods, we linearly vary the duty cycle of the electrodes from 50% to 20% along the 3.6 mm poling length.

The waveguides are fabricated by first patterning a hydrogen silsesquioxane mask using electron-beam lithography. The pattern is transferred to the LN layer by dry etching with Ar^+ plasma to a depth of 350 nm. The etching process yields a characteristic 60° angle of the sidewalls. Finally, the chip facets are polished by first coarse lapping to reach a target of 3 mm unpoled waveguide length between the input facet and poled area, followed by fine polishing to improve the coupling efficiency.

Numerical simulations

The spectral evolution is modelled in the frequency domain with a single-mode unidirectional propagation equation^{28,29} that includes both second- and third-order nonlinearities:

$$i \frac{\partial}{\partial z} a[v] = \left(\beta + i \frac{\alpha}{2} \right) a[v] + \frac{\omega \chi^{(2)}}{\sqrt{\epsilon_0 c^3 n^3 A}} \mathcal{F} \left[a[t]^2 \right] [v] + \frac{\omega \chi^{(3)}}{\epsilon_0 c^2 n^2 A} \mathcal{F} \left[a[t]^3 \right] [v], \quad (1)$$

where $a[v]$ is the spectral amplitude, normalized to the pulse energy $e_p = \int |a|^2 dv$. The linear term includes the frequency-dependent angular wavenumber β and gain/loss parameter α . The nonlinear interactions are calculated in the time domain from powers of the carrier-resolved amplitude and then Fourier transformed (\mathcal{F}) into the frequency domain. Poling is implemented by changing the sign of $\chi^{(2)}$ at the boundary of each domain inversion. The strength of the nonlinear terms depends on the effective refractive index n and mode area A (1.095 μm^2), which were calculated using the mode solvers of Lumerical with the waveguide parameters shown in Fig. 1b and a sidewall angle of 60°. The values of the refractive indices used in the mode solver are from Lumerical. The propagation loss was assumed to be 1.1 dB cm^{-1} and the values used for nonlinear susceptibilities $\chi^{(2)}$ and $\chi^{(3)}$ were 30 pm V^{-1} and 5,200 $\text{pm}^2 \text{V}^{-2}$, respectively. For clarity, the notation has been dropped for the frequency dependence of the waveguide parameters on the right-hand side of the equation. The model is integrated using an adaptive third- and fourth-order embedded Runge–Kutta scheme in the interaction picture (ERK4(3)-IP) (ref. 41), and the full simulation framework is currently implemented in a fork of PyNLO⁴².

Data availability

All data required to reproduce the figures in this paper are available via the University of Colorado CU Scholar at <https://scholar.colorado.edu>.

Code availability

The simulations were carried out using the open-source code PyNLO⁴².

References

- Balac, S. & Mahé, F. Embedded Runge–Kutta scheme for step-size control in the interaction picture method. *Comput. Phys. Commun.* **184**, 1211–1219 (2013).
- PyNLO: Python nonlinear optics. *GitHub* <https://github.com/UCBoulder/PyNLO>

Acknowledgements

This work was supported by the National Science Foundation AST 2009982 (P.S. and C.F.), EECs1846273 (L.L., R.S., Q.G. and A.M.) and QLCI award no. OMA-2016244 (S.A.D. and T.-H.W.); the Air Force Office of Scientific Research FA9550-20-1-0040 (L.L., R.S., Q.G. and A.M.); the National Institute of Standards and Technology (NIST) on a Chip program (S.A.D. and T.-H.W.); and the Jet Propulsion Laboratory, California Institute of Technology, under a contract with the National Aeronautics and Space Administration and funded through the internal Research and Technology Development program RSA 1671354 (P.S. and R.M.B.). Device nanofabrication was performed at the Kavli Nanoscience Institute (KNI) at Caltech. We acknowledge helpful comments on the paper from K. Chang and J. Black and valuable input from S. Liefer in the early stages of this project.

Author contributions

T.-H.W., C.F. and S.A.D. conceived the waveguide designs. L.L. fabricated the waveguides with assistance from R.S., Q.G. and R.M.B. The experiments were performed by T.-H.W. and P.S. T.-H.W. and C.F. developed and carried out the modelling. T.-H.W. and S.A.D. wrote the paper with input, analysis and discussion of the results from all authors. A.M. and S.A.D. supervised the project.

Competing interests

L.L. and A.M. are involved in developing photonic integrated nonlinear circuits at PINC Technologies Inc. L.L. and A.M. have an equity interest in PINC Technologies Inc. The other authors declare no competing interests.

Additional information

Supplementary information The online version contains supplementary material available at <https://doi.org/10.1038/s41566-023-01364-0>.

Correspondence and requests for materials should be addressed to Alireza Marandi or Scott A. Diddams.

Peer review information *Nature Photonics* thanks the anonymous reviewers for their contribution to the peer review of this work.

Reprints and permissions information is available at www.nature.com/reprints.